Large-scale flow visualization of a flapping-wing micro air vehicle

Martinez Gallar, Blanca; van Oudheusden, Bas; Sciacchitano, Andrea; Karasek, Matej

DOI
10.3929/ethz-b-000279239

Publication date
2018

Document Version
Final published version

Published in
Proceedings 18th International Symposium on Flow Visualization

LARGE-SCALE FLOW VISUALIZATION OF A FLAPPING-WING MICRO AIR VEHICLE

B. Martínez Gallar[1], B.W. van Oudheusden[1,a], A. Sciacchitano[1], M. Karásek[1]

[1]Faculty of Aerospace Engineering, Delft University of Technology, Kluyverweg 1, 2629HS, The Netherlands
[a] Corresponding author: B.W.vanOudheusden@tudelft.nl

KEYWORDS:
Main subjects: quantitative flow visualization, near-wake topology, flapping
Fluid: incompressible flow
Visualization method(s): Volumetric Particle Image Velocimetry
Other keywords: Micro Air Vehicle

ABSTRACT: *The aim of this investigation is to provide an experimental volumetric visualization of the near wake topology of the vortex structures generated by a flapping-wing Micro Air Vehicle (MAV) by means of large-scale Robotic PIV. This novel technique implements coaxial illumination and imaging in combination with the use of Helium Filled Soap Bubbles (HFSB) as tracing particles to achieve large measurement volumes of the order of 10 liters. Information of different phases throughout the flapping cycle is obtained by means of a phase-locked averaging procedure. Experiments in both tethered and free-flight conditions have been performed, yielding an unprecedented comparison between the aerodynamics of the two conditions.*

1 Introduction

An increasing interest in the development of Micro Air Vehicles (MAVs) has been seen in recent years due to the wide range of missions where they can be employed: from searching and rescuing activities to security and surveillance applications. These MAVs typically fly at very low speeds or even in hovering conditions, but high maneuverability and flight efficiency are desirable for wind gusts rejection and increased flight endurance, respectively. Different classes of MAVs can be distinguished: fixed wings, rotatory wings and flapping wings. Well-established aircraft design concepts apply to fixed and rotatory wing configurations, but they suffer a detrimental effect on performance when scaled down in size. On the other hand, natural fliers, serving as an inspiration to flapping-wing designs, have shown extraordinary flight capabilities at low Reynolds numbers [4][11]. Thanks to new flow visualizations techniques that have become available (Particle Image Velocimetry in particular), the characteristics of the flow of flapping wings has been better understood, supporting the identification of several unsteady flow mechanisms [14] [19]. The understanding of the flow characteristics of flapping wings and their relation to force generation has been investigated extensively on both natural fliers and flapping mechanisms. Nevertheless, there are still no general models or theories that completely describe the aerodynamics of flapping wings.

Extensive experiments have been carried out in the past using natural fliers such as birds and insects and also using Flapping-Wing MAVs (FWMAVs) or simplified mechanical models that are not able to fly. When referring to natural fliers investigations, one can differentiate between experiments done with either tethered or free-flying subjects. In the first case, the animal is fixated at a certain position resembling its normal flight condition [3]. The second option implies letting the animal fly freely across the measuring space and measure the footprint of the vortex structures generated during the flapping [8]. This involves quite a complex setup which includes extensive training as well as the design of protection for the animal in case laser light illumination is used. Another difficulty of this procedure is to repeat the measurements at the same conditions, mainly due to the

inherent unpredictability of animal behavior. These issues are less critical when mechanical flapping mechanisms or even MAVs are used instead.

Multiple bio-inspired FWMAV designs have been developed worldwide, one of which is the DelFly [6], a biplane MAV designed and manufactured at TU Delft. It has two full-span wings, arranged in cross configuration, that move alternately towards and away from each other when flapping (see figure 1) to generate both thrust and lift, taking advantage of the clap-and-fling wing-interaction effect [1]. The wings of the DelFly are made of 15 micron thin Mylar foil reinforced with carbon fiber stringers that makes the wings highly deformable, a characteristic that was found to enhance significantly the aerodynamic performance of the MAV [12]. It is also equipped with horizontal and vertical tail planes and its corresponding control surfaces, elevator and rudder, which make the DelFly a stable and controllable system relying on tail actuation. The DelFly will be used to study the aerodynamics of flapping wings in this study and the vehicle will be described in further detail in section 3.2.

As in the case of natural fliers, measurements on MAVs can be done in fixed (tethered) conditions or in free flight conditions. The first flow visualization experiments to be carried out with a freely flying flapping-wing robot have been successfully performed on the DelFly [10], proving the methodology that will be followed in this study as well. The main characteristic of this methodology is the combination of stereo-PIV and a control system for autonomous flight in a wind tunnel environment. The research done on the DelFly in fixed conditions is quite extensive. These static measurements are less complex to be performed and, with the help of a force balance, the forces generated by the flapping wings can be measured simultaneously to the flow visualization. This allows valuable information to be obtained of the possible relation between flow behavior and resulting force generation. The PIV research done in previous years on the DelFly has always been limited to planar (2C and stereo) PIV [5][7], so information is restricted to a plane. One option to obtain three-dimensional information on the flow structure is to measure different planes subsequently, and synchronize the data of the different planes with the flapping phase. Evidently such an approach requires extensive measurements to be performed and a careful synchronization and interpolation of the datasets. A simpler but more approximate approach reconstructs the three-dimensional structure of the wake from the time-resolved data obtained in a single wake plane, by using a convection model (Taylor's hypothesis), as has been done for the DelFly by Percin et al. [13]. This approach assumes that the wake structures generated by the flapping wings of the DelFly are convected with a velocity equal to the free stream, neglecting the induced velocities produced by the acceleration generated by the clap-and-fling and the wake vortices themselves. This assumption may be reasonable for a zero angle of attack forward-flight configuration, allowing to visualize the main structures that can be seen in the wake, which include mainly the tip vortices generated by the four wings and the starting trailing edge vortex connected to the tip vortex. With this technique it was also possible to assess the interaction between the vortex structures at different reduced frequencies. It was concluded that an increase in reduced frequency leads to a stronger interaction between the vortices, which is linked as well with the enhancement of clap-and-fling mechanism. However the use of Taylor's hypothesis fails to represent the wake at realistic flight conditions where the angle of attack is quite high and so the interaction between the velocities induced by the wings and the free stream is too complex to be accounted for by the simple convection model underlying the Taylor's hypothesis.

These arguments evidently suggest that a reliable characterization of the flapping-wing flow field requires a volumetric visualization approach. Volumetric Tomographic PIV has been used to reconstruct the wake of a desert locust in tethered conditions by Bomphrey et al. [2]. The measuring

volume that could be achieved by this technique was limited to a thickness of 4 mm, measured in the longitudinal direction, to be able to cover all the wake in width and height. The small thickness makes the use of Taylor's hypothesis inevitable to propagate the flow information downstream in order to describe the full wake, and a further analysis of the results shows indeed that the use of Taylor's hypothesis introduces errors on wake morphology, which can lead to erroneous force calculations based on such information. To correct for this, wake deformation was considered in this case by looking at the angle of the Q-criterion iso-surfaces and matching them from one measurement to the next. With wake deformation applied, the shape of the wake structures was found to change significantly. This leads to the conclusion that volumes captured at subsequent time intervals do not reliably compose the actual wake shape and a large volume imaging technique would be desired that can properly capture the longitudinal extent of the wake. This cannot be achieved by regular tomo-PIV as discussed by Scarano et al. [15], however, in view of the volume restrictions.

To overcome these limitations, in the current study large-scale Robotic Volumetric PIV was used instead of regular stereo or tomo-PIV, employing helium-filled soap bubbles (HFSB) as flow tracers, which permits to visualize the entire 3D wake structures without necessity to rely on any hypothesis to reconstruct them. The setup was subsequently used to investigate the wake structure of the DelFly in both tethered and free-flight conditions, at different values of the (effective) flight speed.

2 Experimental procedures

A DelFly vehicle was used as the experimental object in the present study. Wind tunnel experiments were performed in two different campaigns, one with the DelFly model in tethered conditions and another with the complete DelFly vehicle in actual free flight. For the first set of experiments, the selected configurations aim to represent the same conditions as the DelFly would have in free flight, by setting appropriate values of three relevant parameters, which are: the flight speed (U_∞), the flapping frequency (f_{flap}) and the angle of attack (α_b) of the body with respect to the free-stream. The complete setup of the experimental campaign is presented in the following sections, starting with the MAV (Sec 2.1) that has been used and continuing with the different facilities where experiments were performed in sections 2.2 and 2.3. To finalize, the complete Robotic PIV system will be presented (Sec 3.4).

2.1 Full-scale DelFly system

The DelFly MAV used in the experiments is the most recent design. The lay-out and dimensions of a half-wing of the MAV can be seen in figure 1. The weight of the DelFly is approximately 25 g and the distance from the leading edge of the wings to the trailing edge of the tail is 21.5 cm approximately. The total span of the wings is 28 cm while the tail has a span of 17 cm. The tail is painted black for the experiments to avoid unwanted reflections from its surfaces. Unfortunately, this could not be done for the wings of the DelFly as the paint could change considerably the stiffness and the weight of the wings. As the laser light reflections from the wings would present an obstacle in the processing of the images, for this reason the flow around the wings has not been studied.

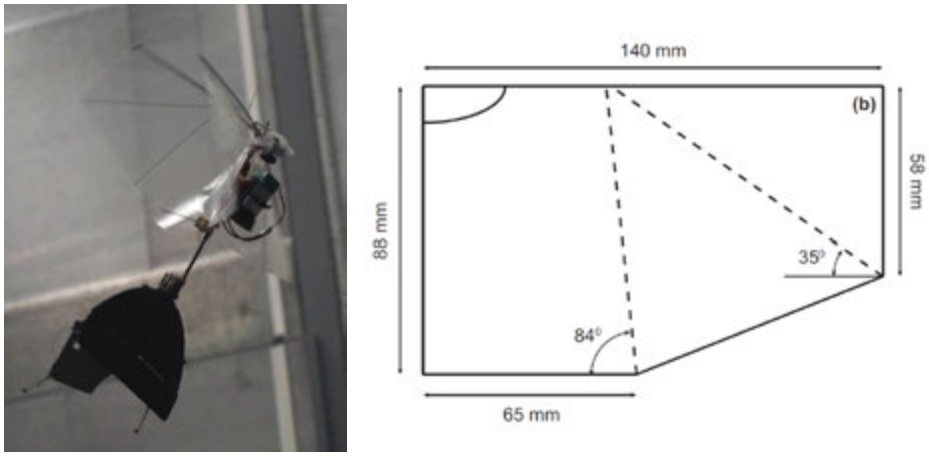

Fig. 1. The Delfly MAV used in the experiments (left) and the dimensions of a single half-wing, including the location of the stiffeners (right)

2.2 Wind tunnel setup for tethered experiments

The tethered experiments were performed in a low-speed wind tunnel at the Aerodynamic Laboratory of TU Delft, which has an open test section with cross-sectional dimensions of 60 cm × 60 cm and a contraction ratio of 3.62. The distributor providing the HFSB seeding particles was placed in the settling chamber, upstream of the test section. The measurements were performed at free-stream velocities (U_∞) in the range of 0.5–2 m/s. With the mean wing chord length being c = *80 mm*, the corresponding Reynolds number ($\mathrm{Re} = U_\infty c/\nu$) ranges from 2,800 to 11,300.

The DelFly was positioned in the middle of the wind tunnel, supported by a structure that allows to set the desired body angle of attack (figure 2). A Hall-effect switch, installed next to the magnet-equipped output gear of the DelFly gearbox, gave the necessary information about the wing position by providing a pulse signal every flapping cycle. By means of highspeed camera recording, the system was calibrated to know the position of the wings, and hence the phase in the flapping cycle, when the pulse signal was sent. The power input for the DelFly is controlled to achieve a constant flapping frequency, which is varied from 10 to 13 Hz.

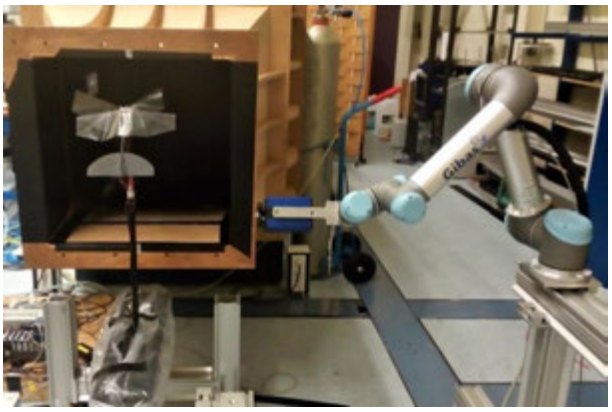

Fig. 2. Experimental setup tethered conditions

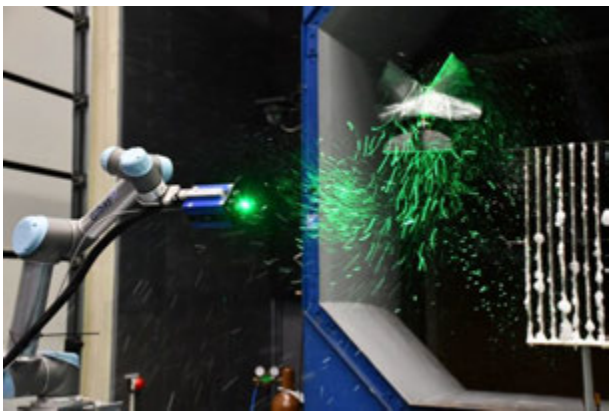

Fig. 3. Experimental setup free-flight conditions

2.3 Wind tunnel setup for free-flight experiments

The second experimental campaign was performed in the Open Jet Facility (OJF) of TU Delft, which is a relatively large-size wind tunnel with an open test section of 2.85 × 2.85 m^2 cross section, and a contraction ratio of 3. The seeding generator is in this case placed directly after the wind tunnel contraction as can be appreciated in figure 3. In the picture it can be observed that the setup of the Coaxial Volumetric Velocimeter (CVV) and the robotic arm is very similar to the one used in the first campaign. The main difference is encountered with respect to the positioning of the DelFly, which in this case is flying in the open test section of the wind tunnel without any support. The DelFly position is controlled by an on-board autopilot, which steers the vehicle based on feedback from the on-board IMU (used for attitude estimation) and from an external motion tracking system that provides position and heading information (with respect to ground) [10]. The external motion tracking system employs 12 OptiTrack Flex 13 cameras (NaturalPoint, Inc., resolution 1280 px × 1024 px, 120 fps). The tracking system data is collected to determine the wing position and the location of the DelFly throughout the measurement. This provides the information on the flapping phase of the wings required in the phase-averaging procedure, while also allowing to apply corrections on the measured data to account for the dynamic motion of the DelFly. More information on the DelFly control system and the data synchronization with the PIV dataset can be found in [10].

2.4 Robotic PIV equipment

2.4.1 Coaxial Volumetric Velocimetry

The investigation uses Robotic Volumetric Velocimetry as a visualization technique, which allows measurement of the three components of velocity in a large volume (of the order of several liters). The optical component of the measurement system (Coaxial Volumetric Velocimeter, CVV [18]) makes use of a coaxial arrangement between imaging and illumination. It contains four cameras arranged in a cross configuration and a laser light source located in the center of the four cameras (see figure 4). The light is emitted by the laser head and conveyed to the center of the CVV system via an optical fiber. The use of the laser optics enables the laser light to spread through space with a conical shape. In the Robotic Volumetric Velocimetry system, the CVV module is mounted on a robotic arm to move it to the desired measuring position with high precision. The advantages of this compact and robotically actuated device are mainly the improvement in optical access, the saving in time as only one calibration is needed and the fact that measurements can be repeated in adjacent volumes to achieve a total measurement domain of the order of 100 liters.

The Robotic Volumetric Velocimetry system is used in combination with Helium Filled Soap Bubbles (HFSB) [16] as flow tracers. The HFSB are sub-millimeter neutrally buoyant particles that scatter light with much higher intensity than conventional micron-sized particles. As a result, the HFSB are visible even when the illuminating laser light is spread over a cross section of the order of 1,000 cm^2, thus allowing the large volumetric visualization capability of the CVV approach to be exploited.

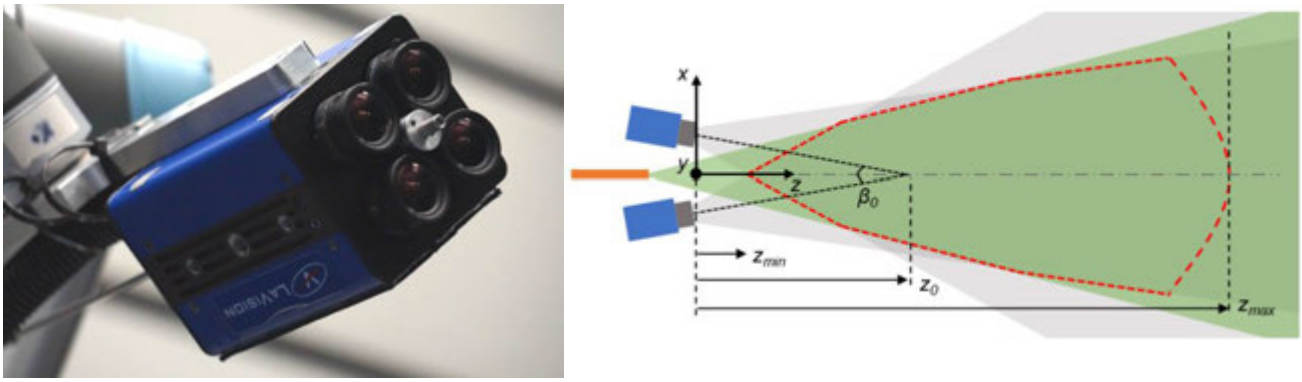

Fig. 4. Measurement setup *(left)* and operating principle *(right)* for the coaxial velocimeter (CVV), showing cameras (blue), field of view (grey) and laser illumination (green) provided by the optical fiber (orange); the red dashed line describes the effective measurement cone [Schneiders PhD thesis]

2.4.2 PIV experimental setup

The Robotic PIV system is composed of three major parts: the HFSB seeding generator, the Coaxial Volumetric Velocimeter (CVV) [9] and the robotic arm. The seeding generator is composed of 10 wings with 20 seeding nozzles each, with a total cross section of 50 × 100 cm^2 and a nozzle pitch between generators of 5 cm in both directions. For the tethered experiments, the seeding generator is placed in the settling chamber of the wind tunnel to minimize the increase of free-stream turbulence. After the wind tunnel contraction, the seeded stream-tube covers a region of about 30 × 55 cm^2 all around the DelFly. In the case of free-flight experiments, the seeding generator is placed after the contraction, so the seeded stream tube has a cross-section of 50 × 100 cm^2.

The CVV system is composed of four CMOS cameras close together at low tomographic aperture ($\beta_0 = 4°$). The illumination is provided by a Quantronix Darwin Duo Nd:YLF laser via an optical fiber located in the middle of the cameras. The cameras recorded 8000 images per cone acquired at a rate of 471 Hz in continuous mode for all the measurements performed. The images need to be pre-processed before the particle tracking algorithm can be applied due to the reflections generated by the body and wings of the DelFly. The approach followed to eliminate the reflections is to apply a Gaussian smoothing to spread the reflection area along the different images so then it can be easily removed by a Butterworth filter. The measuring time per sequence is 17 seconds which corresponds to approximately 200 wingbeats, with 40 images recorded for each wingbeat, assuming a flapping frequency of 12 Hz. The CVV system records images in a conical volume of about 20 cm in height and width, and 30 cm in depth. Five repeated measurements were taken for each conical volume (resulting in 40,000 images in total). A Universal Robots - UR5 robotic arm is employed to move the CVV position in space with millimetric precision.

In order to measure the entire wake of the DelFly wings, several conical volumes were taken for the same configuration at different locations; the information obtained for the different cones is then combined together with an in-house Matlab code. Four different conical volumes are taken in total which can be seen in the graphical representation in figure 5, the volumes are not accurately scaled with the DelFly. The depth direction of the cameras was placed in the spanwise direction of the DelFly, as shown in figure 3. The CVV was moved in the longitudinal plane, i.e. normal to the spanwise direction. One pair of cones was needed to visualize the upper and lower parts of the Delfy. In addition, two consecutive pairs of cones were taken along the body direction of the DelFly to capture the length of the wake. The dimensions of the total measuring volume amounted to 50 cm × 30 cm × 40 cm (in x, y and z-direction, respectively).

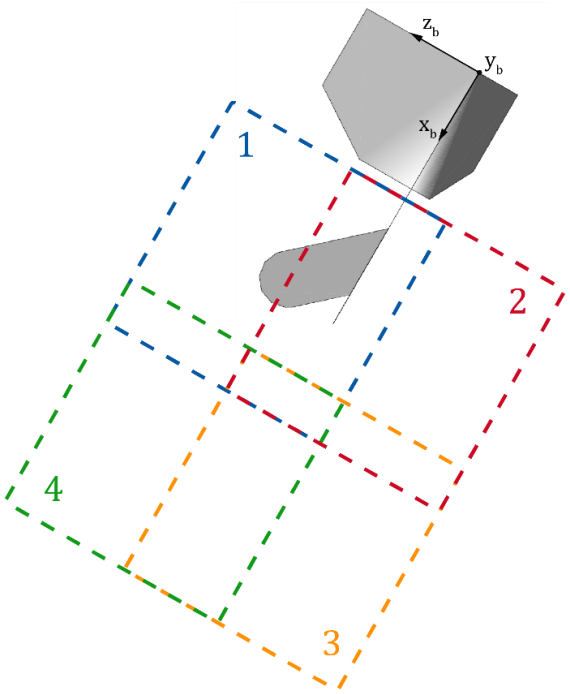

Fig. 5. Set of volumes that are combined to create the total measuring volume of the experiment

2.4.3 Particle tracking algorithm

The CVV system records the particles intensity in the images and by means of Particle Tracking Velocimetry (PTV) the velocity information of the flow is extracted from the images. The information about the location of each particle in time is determined in a Lagrangian way, where the Shake-the-Box (STB) algorithm [17] is employed to reconstruct the particle trajectories. With the information of the location of the particles in time, a second order polynomial fit is used to compute the particle velocities. This technique is several orders of magnitude less demanding in terms of computational time than the tomographic PIV technique, due to the fact that the volume reconstruction is particle-based instead of voxel-based, and that no cross-correlation analysis is conducted. The output of the Shake-The-Box processing is the information of the tracks that the particles have followed in time. The number of particles captured at each time instant, and therefore the track density in the measurement domain, is usually not large enough to achieve instantaneous velocity fields with sufficient spatial resolution to resolve the main flow structures. Therefore, a time averaging needs to be applied to increase the density of particle tracks in the measurement domain.

Due to the flapping motion of the wings, the flow is highly unsteady and a pure time-average representation of the flow is not meaningful. However, the flow evolves through a periodic flapping cycle, generating different vortex structures on the instroke (wings going towards each other) and the outstroke (going away from each other). With the measurement technique used, the cyclic evolution of the flow can be obtained by computing phase-averaged flow fields that correspond to different phases in the flapping cycle. Information about the wing position through time, correlated with the recording of the images, becomes crucial for the success of the phase-averged flow visualization. To achieve a better accuracy at each phase, the information from one time step to the following one is interpolated to get the information at the exact time when the wings are at a specific location. Finally, the flow results that are originally obtained in a Lagrangian (unstructured) representation are converted into a Eulerian one to obtain a three-dimensional grid that relates to the

measured volume, and which facilitates graphical display of the results. The posibility to combine different measurement volumes to increase the total space analyzed is exploited.

3 Results

The current section reports the evolution of the vortex structures through a flapping cycle. First, the velocity results are discussed in wake planes oriented perpendicular to the body axis (section 3.1) to explain the main features of the wake topology of the DelFly. Second, the differences between two different configurations in tethered conditions are assessed in section 3.2 to analyze the effect of reduced frequency on the wake structures. Finally, a comparison between the results at similar configurations between tethered and free-flight conditions is performed in section 3.3. The main parameters for each of the considered configurations, labelled as A, B and C for convenience, can be found in table 1.

Table 1. Flight parameters for each configuration and the corresponding reduced frequency

Configuration	Experimental conditions	$U_\infty\ [m/s]$	$f_{flap}\ [Hz]$	α_b [°]	$k = \pi f_{flap} c/U_\infty$
A	Tethered	0.5	13.0	70	6.5
B	Tethered	2.0	10.2	31	1.3
C	Free-flight	2.0	11.4	30	1.4

3.1 Wake topology during a flapping cycle

From the data measured for configuration B, information is extracted in a wake plane that is located 10 mm downstream of the trailing edge of the DelFly tail. All information is shown in a body reference frame, with the x-component set along the body of the DelFly and y the spanwise direction (see also figure 5). In all the plots, the position of the DelFly is indicated in black to relate the flow field results with the position of the wings. The flapping cycle has been divided into eight phases to show the behavior of the flow structures and their evolution over the flapping cycle. The flapping cycle is set to start when the wings are closed and the outstroke is going to start. Note, however, that this wing position is virtual with respect to the flow fields, as the flow measured is not corresponding to the position of the physical wings at that precise moment, in view of the convective delay between the wing position and the visualization plane. The wing position has been deduced from the information of the change in crossflow velocity along the wingbeat. In the setup of these experiments, the CVV system was positioned at the right-hand side of the DelFly (i.e. positive y, see figure 3) which leads to a better tracking of the particles on that side of the DelFly, because the particles that are closer to the laser source will scatter more light as the intensity decreases with the fourth power of the distance. At the end, having more particles tracked contributes to a higher accuracy in that measuring side.

Regarding the acceleration region, represented by the red areas of high longitudinal velocity, its evolution along the flapping cycle is presented in figure 6. The first phase (figure 6-I) of the cycle is presented when the outstroke is just starting. There is no clear acceleration region in the wake of the DelFly, because the wings are closed. It is seen in figure 6-II that a high-velocity region has drastically increased from the previous phase due to the opening of the wings. The deformation of the wings plays a major role in this effect due to the “peeling” action (see figure 7).

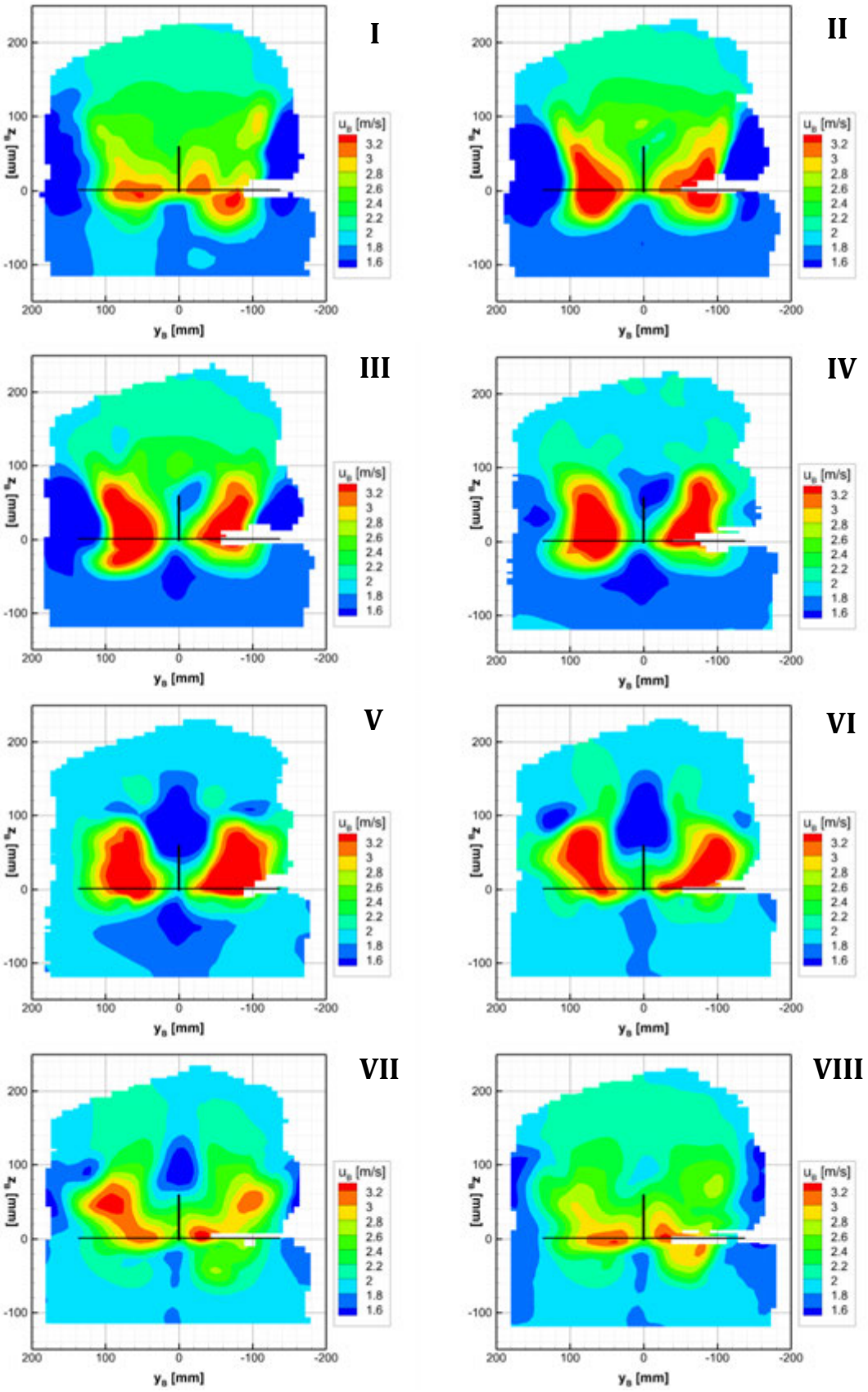

Fig. 6. Contour plots of the velocity component on the body direction in a spanwise oriented plane at 10 mm distance from the end of the tail at 8 phases along the flapping cycle for configuration B

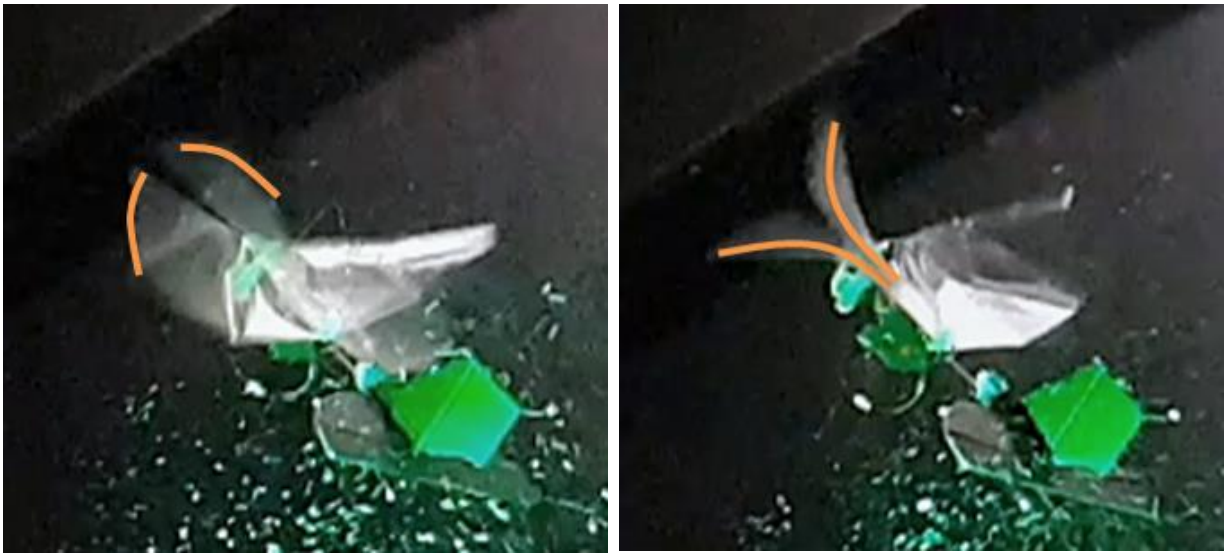

Fig. 7. Deformation of the wings of the DelFly enhancing the clap (left) and peel (right) mechanisms

The acceleration region keeps increasing during phases III and IV as the wings are still opening further. On phase V, when the instroke has started, the acceleration that is generated by the wings reaches its maximum, again due to the deformation of the wings and the "clapping" effect that is created as the wings move together (see figure 7). On the following phases, from VI-VIII, the acceleration region reduces its size and it is concentrated into two different regions, one near the body of the DelFly and the other near the tip of the wings. The flow at the first location follows the direction of the body while the second acceleration region has a lateral component of velocity directing the flow outward along the wings (figure 8). The outward velocity occurs as a consequence of the deformation of the wings. The deformation along the wing is restricted because of the presence of the stiffeners as shown in figure 1; this may be why the acceleration region at the end separates in two. In the most outward part of the wing, apart from the expected chordwise deformation, there is a spanwise deformation of the wing which is a probable cause of the observed acceleration of flow in the lateral direction.

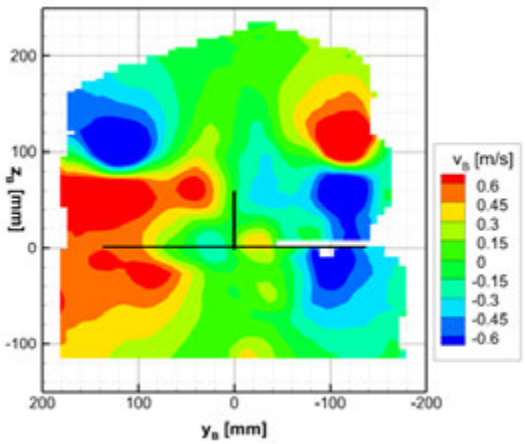

Fig. 8. Contour plot of the lateral velocity component in a spanwise oriented plane at 10 mm distance from the end of the tail at phase VII of the flapping cycle for configuration B

Figure 9 displays the longitudinal vorticity (i.e. in the direction of the MAV body axis) for subsequent phases of the flapping cycle. The first observation is that there are two main counter-rotating vortices originating from the tips of the DelFly during the entire flapping cycle. According

to simple lifting line theory, this implies that positive lift is generated during the entire flapping cycle, which is crucial for the MAV to provide the necessary lift in order to maintain its altitude. Lift is defined as the force generated perpendicular to the free stream, so the vertical force in an absolute reference frame. The vortices are shed by the lower pair of wings during the outstroke and by the upper wings during the instroke. This finding leads to the conclusion that the main vortices are always shed by the wing that is moving in the direction opposite to that of the freestream, when the relative velocity of the wing with respect to the flow is higher and the majority of the force is generated. When looking at the wings moving along with the flow, the velocity experienced by the wing surface is reduced significantly. Assuming that the effective rotational velocity produced by the wing is located at two thirds of the wing span ($b = 14\ cm$), it is estimated that the total velocity seen by the wing moving against the flow is more than three times larger than the one seen by the wing going in the freestream direction.

Looking more in detail to the different phases, two strong counter-rotating tip vortices are retrieved in phase I of the cycle (starting of the outstroke) that are generated by the upper wings during the previous instroke. These tip vortices (wake structures A in figure 9) interact with the wings while they are closed and then with the tip vortices generated by the lower wings during the outstroke, resulting in a major tip vortex structure with the same sign for the entire cycle, as it can be clearly appreciated in the 3D view that will be shown in section 3.2. The tip vortex structure in phase II is quite elongated, as it is also the case for phase III. The shape of the tip vortices along the outstroke will be further discussed in section 3.2. Several smaller vortices start to appear in phase II but they are not yet defined until phase III, named B in the figure. The crossflow going over the wings from tip to root needs to be redirected once it reaches the root, generating these vortices.

In phase IV the wings are completely open and the instroke is starting. According to lifting theory, a lifting surface of finite span will generate tip and root vortices at the extremities of the surface, that are aligned with the freestream direction. This same concept can be applied to flapping wings, similar to propeller theory. In this way when the upper wings start to generate lift, a spanwise-aligned starting vortex is produced that is followed by the generation of counter-rotating tip and root vortices. From figure 8-IV and 8-V, the evolution of root and tip vortices can be confirmed (wake structures C and A respectively in figure 9). To be able to locate the starting vortex, contour plots of y-vorticity are analyzed. In figure 10 such plot for phase V is presented, where the starting vortex can be seen at the upper side of the DelFly. The vorticity in that region has a negative sign which means that positive circulation, and therefore positive lift is being generated. The starting vortex can only be clearly seen at the beginning of the instroke because at the beginning of the outstroke a strong interaction between the wings occurs so the change in circulation of the wings is not significant. On the lower side of figure 10, however, the opposite behavior is found in a large area with high positive y- vorticity. It corresponds to the trailing edge vortices shed from the lower wings when they stop producing lift. The trailing edge vortex generated by a lifting surface is indeed of opposite sign of that of the starting vortex.

In phase V the wings are completely open, which causes the crossflow along the lower wings to be maximum, hence, the secondary vortices formed on the upper part of the DelFly are enhanced. Then the peak vorticity of these vortices diminishes drastically when the wings come closer together as the flow is now directed away from the root, and towards the tips. In the same way the root vortices also experience a decrease in strength and they nearly disappear at phase VIII as the wings are approximately closed and the DelFly resembles a fixed wing vehicle. The tip vortices, where the highest rotational velocity can be found, are still maintaining their strength throughout the final phases of the cycle.

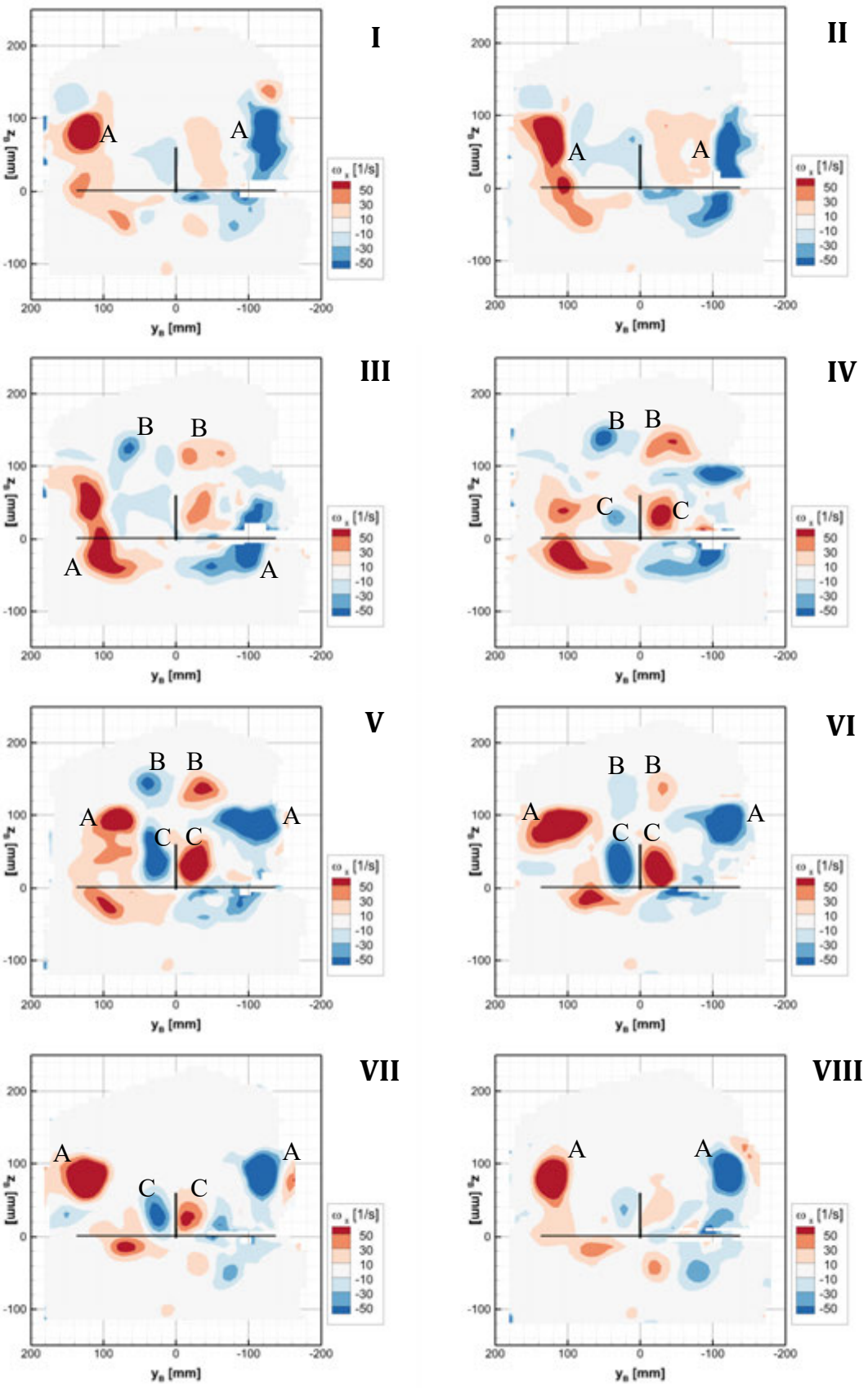

Fig. 9. Contour plots of the out-of-plane vorticity ω_x in a spanwise oriented plane at 10 mm distance from the end of the tail at 8 phases along the flapping cycle for configuration B

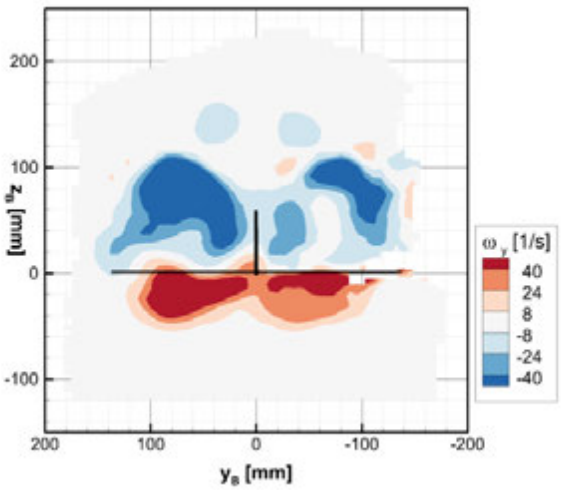

Fig. 10. Contour plot of the on-plane vorticity ω_y in a spanwise oriented plane at 10 mm distance from the end of the tail at phase V of the flapping cycle for configuration B

3.2 3D wake topology

Considering again configuration B, the vortex structures explained in the previous section are now discussed by means of their 3D representation. Note that although data is available for the full span of the wake, only the structures at one side (corresponding to positive y) are depicted to facilitate the visual interpretation. The development of the topology obtained for different phases of the cycle is sketched to give an overview of the variation of the structures while they are convected. In figure 12 the different vortices are identified and the distinction between instroke and outstroke is also presented. The division between instroke and outstroke has been done by visual inspection of the vortical shape in accordance to the reasoning presented in section 3.1, so this distinction is primarily meant as a guideline to understand the observed phenomena. It may be reminded here that the x-axis is aligned with the body axis, so the upward deflection of the wake that can be observed in the side view of figure 12 is the result of the body angle with respect to the freestream direction ($\alpha_b = 31°$ in this case).

The large tip vortex structures that were already explained in section 3.1 can be clearly seen in figure 12. The shape of the convected tip vortex seems to be straight with respect to the DelFly body during the instroke while it is deflected downwards during the outstroke, which was also seen in figure 9 on phases II and III. During the outstroke, the lower wing is the one that is generating the tip vortex, which agrees with the downward movement of the vortex. Another reason for the shape of the vortex on the outstroke comes from the fact that the convection velocity is lower in this part of the cycle, especially in the tip area where air is being redirected towards the root. Therefore, the vortex does not travel away along the x-direction in the first stages of the outstroke. Indeed, the vortex is moved slightly towards the center of the DelFly due to the crossflow that appears. This also explains the fact that the instroke structures are longer in space than the ones generated during the outstroke (the gray area is shorter than the white area).

The wake topology is highly affected by the different convection velocities that are experienced throughout the flapping cycle in different locations around the wings (figure 6). This makes the analysis of the wake evolution more complex. The vortices generated by the flapping wings are not convected in the direction of the body of the DelFly, neither in the direction of the freestream. There is a combination between the freestream and the effect of the induced high-speed flow generated through the cycle. The result is a certain angle of the wake that varies as the structures

travel away from the wings which means that the importance of the acceleration jet decreases and the wake convection velocity will become more uniform and closer to the freestream velocity. However, this point is not reached within the measuring volume studied and, instead, it will be assumed that over the measured region the angle of the wake is approximately constant. The value of this wake angle is computed by taking the information of the wake at two different spanwise oriented planes that are spaced in the x-direction, such that they correspond to the same phase of the flapping cycle. A correlation between the x-vorticity values of both planes gives the displacement of the vortex structures during the length of a flapping cycle. This procedure is carried out for each of the eight phases shown in section 3.1. The result for each phase varies, so only the correlations with a signal to noise ratio $SNR > 2.9$ are considered. The mean angle of the wake with respect to the longitudinal body direction is established to be approximately 15 degrees, which agrees with a visual inspection looking at the side view in figure 12. The angle of the wake in the lateral direction is not so easily visualized. The cross correlation procedure computes an outwards movement of the wake structures with an angle of 2 degrees. The outward velocity that was presented in the previous section has an influence on the movement of the wake which slightly moves away from the center of the DelFly.

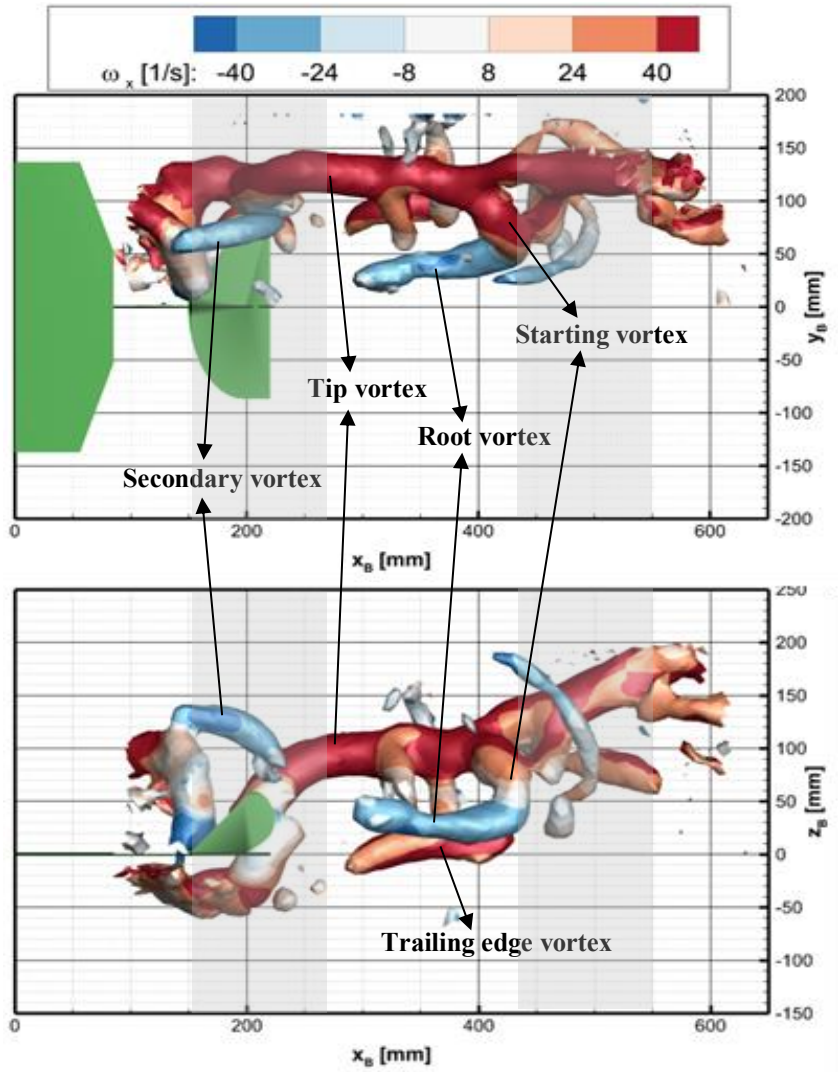

Fig. 12. Top and side views of the wake structures of configuration B, visualized by isosurfaces of Q=600 and colored by ω_x for phase II divided in outstroke (gray area) and instroke (white area)

The evolution of the wake at three different phases during the flapping cycle can be seen in figure 13, where the plane location corresponding to the information depicted in section 3.1 is also indicated (orange line). The assumption of a constant wake angle seems to be reasonable when looking at the side views of the different phases. Starting from phase II that has been explained in detail before, phase V shows clearly the starting vortex linked to the root and tip vortices during the instroke. The secondary vortex created during the outstroke moves upwards and inwards, respectively in the side and top views. As it can only be expected, the vortex structures become more diffused as they are convected which can be clearly seen when looking at the root vortex from phase II which is not seen so clearly in phase V. The peak vorticity of all vortex structures also decreases. On phase VII the vortex structures from the instroke have moved downstream and the trailing edge vortex from the lower wings is seen below the root vortex. The secondary vortex seems to interact with small vortices generated before. This interaction probably originates before this point but the reason behind this interaction has not been studied in detail.

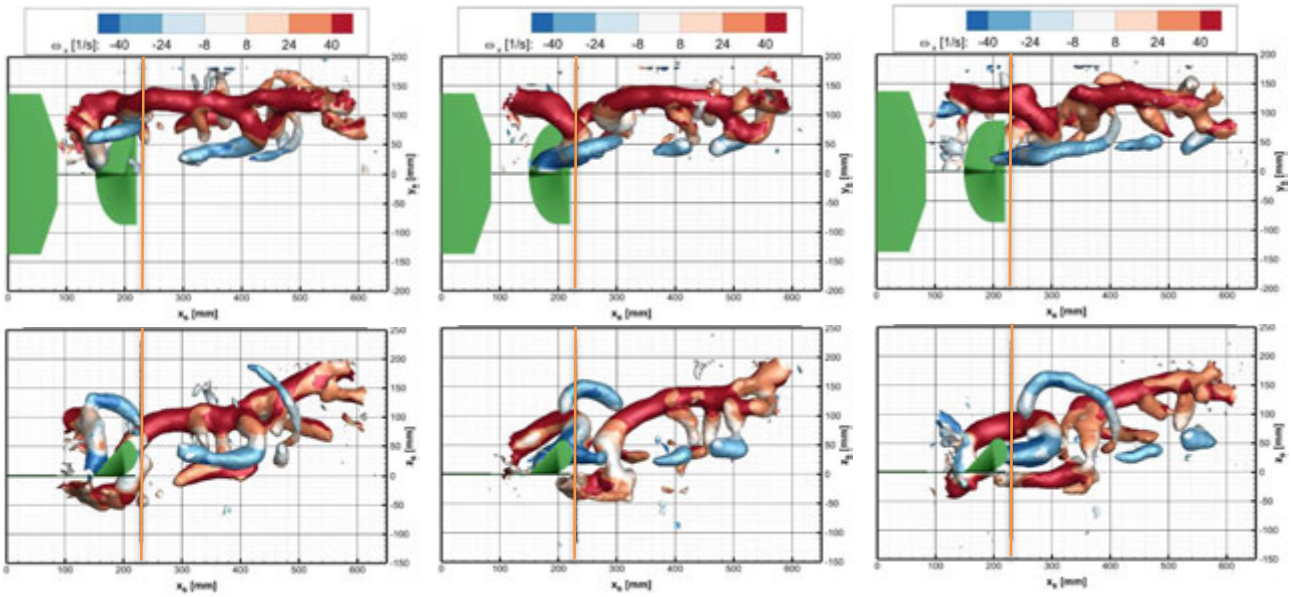

Fig. 13. Top and side views of the wake structures visualized by isosurfaces of Q=600 and colored by ω_x for phases II (left), phase V (center) and phase VII (right) of configuration B

3.3 Effect of reduced frequency

From previous studies [12], it has been concluded that the interaction between the vortices in the wake of a flapping wing system is influenced by the reduced frequency of the system. To investigate this effect, configurations A and B will be compared, where the reduced frequency of configuration A is five times higher than the one of configuration B (table 1). The difference between the two configurations are assessed both qualitatively and quantitatively.

The 3D wake topology for both configurations is presented in figure 14. There are large differences between the two topologies shown, but some similarities can still be observed. The major vortex structure appreciated in both configurations is the tip vortex. The tip vortex in case A is no longer a smooth structure throughout the flapping cycle, but it has a distinct shape for instroke and outstroke. During the instroke, the tip vortex and the starting vortex cannot be distinguished, forming a single oblique vortex (see top view) that starts close to the root of the DelFly and moves outwards as the instroke develops. The tip vortex generated during the outstroke is shorter, as it was the case for configuration B, and it follows a straighter path with respect to the body of the MAV. A second tip vortex structure generated during the instroke on the lower part of the DelFly can be seen in the side

view for configuration A. This indicates that the lower wing is producing lift. However, the x-vorticity of this structure is negative, which indicates that negative lift is being generated. This can be confirmed from analyzing the y-vorticity which has positive values for the lower wing during the instroke (figure not shown as it is similar to figure 10). But in this case it is not the trailing vortex that is shed but the starting vortex of a sudden change in lift generation. The strength of this vortex is smaller than the one measured for the tip vortex of the upper wing, so the resulting force generated by the DelFly is still positive. Another vortex structure that appears for configuration A is located on the upper part of the instroke tip vortex looking at the side view. This vortex is not present close to the wings, but as the wake travels downstream the vortices interact strongly with each other. The outstroke tip vortex seems to interact with the tip vortex of the following instroke.

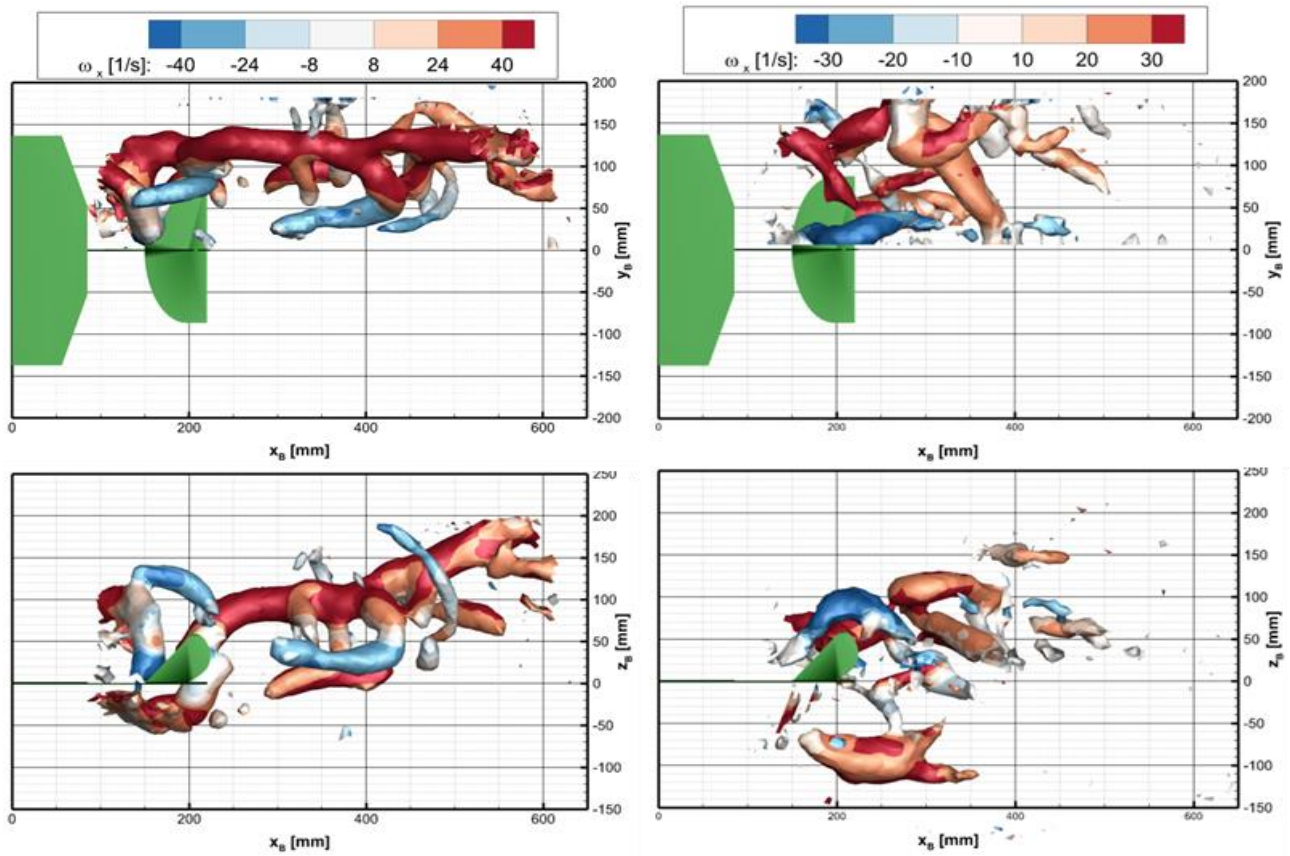

Fig. 14. Top and side views of the wake structures visualized by isosurfaces of $Q = 250$ (right) or $Q = 600$ (left) and colored by ω_x for phases II of configurations A (right) and B (left)

No root vortex is observed in configuration A for any of the wings at any phase of the flapping cycle. Due to the relatively high flapping frequency, the flow at the root of the wings is constantly changing and the dominant component is the crossflow. The secondary vortex should have a higher peak vorticity due to this reason as well. The secondary vortex is generated closer to the root than in configuration B in both y- and z-direction. The fact that it is closer in the z-direction is likely due to the free stream component in configuration A being much smaller than for configuration B so the convection of the vortices is much more influenced by the flow acceleration induced by the wings. This causes the angle of the wake with respect to the body to be smaller. However, it is difficult to give a conclusive statement on that aspect, as the wake length that could be reliably resolved in configuration A is smaller than for configuration B (compare the two cases in figure 14), for a number of reasons. Firstly, the vortex structures are weaker in this case, so they fade away much faster and become more difficult to detect. An additional matter is the larger angle of the body with

respect to the freestream direction ($\alpha_b = 70°$ in this case), so the wake more quickly interacts with the shear layer of the open test section of the wind tunnel. Also, the high body angle brings the wings closer to the supporting structure, which may affect the flow and the measurement of possible vortices generated by the flapping wings on the lower side of the DelFly.

To provide a more quantitative view of the differences between the two configurations, several parameters have been measured: the wake length of a flapping cycle, the maximum longitudinal velocity, the peak vorticities on x- and y-directions and the angle of the wake with respect to the body axis of the DelFly. The information has been collected in table 2. The wake length of a flapping cycle has been computed by determining the difference between the location of the start of the instroke which is defined as the time when the starting vortex is shed. This length is retrieved by visual means from the flow visualization results to give an approximate length, not as an exact measurement. The values of maximum velocity and vorticity are computed by selecting only a region where more that 1200 particles have been tracked on the same slice as the contour plots shown in section 3.1. Unfortunately, the resulting values of the wake angle for configuration A were not conclusive mainly since the wake structures change rapidly which does not allow to use the technique that is used in configuration B.

Table 2. Flight parameters for each configuration and the resultant wake parameters obtained

Conf.	U_∞ $[m/s]$	f_{flap} $[Hz]$	α_b [°]	Length of cycle $[cm]$		$U_{b_{MAX}}$ $[m/s]$	$\left(\frac{U_{b_{MAX}}}{U_\infty cos(\alpha_b)}\right)$	$\omega_{X_{MAX}}$ $[1/s]$	$\omega_{Y_{MAX}}/\omega_{Y_{MIN}}$ $[1/s]$
				Measured	Taylor's hyp.	at $x_b = 23\ cm$			
A	0.5	13.0	70	16	1.3	1.5	(8.6)	77	42/-129
B	2.0	10.2	31	27	16.8	3.8	(2.2)	142	107/-145

The value of the length of the flapping cycle following from Taylor's hypothesis has also been calculated for comparison. According to this approach the wake structures are convected at the free stream velocity. Since the DelFly is positioned at a certain angle of attack, only the free stream component directed along the x-body axis is considered in order to retrieve the wake length in x-direction. This gives a corresponding expression for the wake length as: $U_\infty cos(\alpha_b)/f_{flap}$. As seen in table 2, the length computed with this hypothesis is (much) shorter than the actual wake length measured, which implies that the effective convection speed is higher than predicted by Taylor's hypothesis. For configuration B, the difference between the two is approximately 38% of the measured wake length. This difference is caused by the increased convection speed resulting from the high-speed jet generated by the flapping wings, as previously discussed. The maximum velocity of the jet, $U_{b_{MAX}}$, is more than twice the free stream velocity. The difference between the wake lengths for configuration A is much more dramatic, reaching a 92% difference. This proves the invalidity of Taylor's hypothesis for reduced frequency situations, when the high-speed jet provides a strong flow acceleration, which occurs at higher flapping frequencies in combination with low forward velocities. From the observed wake length and the flapping frequency, an effective (average) convection velocity can be derived, which yields 2.08 m/s and 2.75 m/s for configurations A and B, respectively, indeed well in excess of the corresponding freestream velocity.

The maximum values of x-vorticity (ω_X) is found always in the tip vortex structure across al phases analyzed. The maximum value for configuration B is much larger than the one of configuration A as more force is generated on the wings for the first one. The overall maximum value along the flapping cycle is found at the beginning of the outstroke, which corresponds to phase II for configuration B, while for configuration A it occurs at phase III. This indicates a probable phase lag of the wake structures generated by the flapping wigs. This phenomenon was already discussed by

Percin et al. [Percin2016]. The maximum is reached when the wings are close together and coming apart from each other, which can relate to the interaction of the tip vortex from the previous instroke that combines its strength with the following vortex generated by the lower wing.

Considering the y-vorticity (ω_y), both the maximum and minimum values are important. On the right side that is being evaluated, a positive peak y-vorticity indicates the presence of trailing edge vortex or just a sudden change in lift generated which happens during the instroke on the lower wing. A negative y-vorticity peak on the other hand will show the location of the starting vortex generated by the upper wing in the instroke. Both are generated at the same phase, being phase V according to configuration B and phase VI for configuration A. This reinforces the idea of a phase lag between the configurations. The magnitude of the peak vorticity of the starting vortex is larger than the one of the trailing edge vortex, which means at the end that the overall lift generated is positive. The value of vorticity of the starting vortex does not differ so much as in the case of the x-vorticity. The lift that should be generated by both wings at the end should be quite similar as the weight that needs to be supported is the same.

3.4 Free-flight vs. tethered conditions

To finalize the analysis, a comparison between tethered and free flight experimental conditions is investigated using configurations B and C. The reduced frequency for both cases is very similar, albeit that the flapping frequency for case C is slightly higher than for case B, approximately 10% difference is found. This appears to influence the length of the wake for a flapping cycle, as it could be expected. The length of the wake is approximately 27 cm and 24 cm for configurations B and C respectively, as seen in figure 15, which is consistent with the difference in flapping frequency. The vortex structures that can be appreciated for free-flight are not captured with the same level of detail

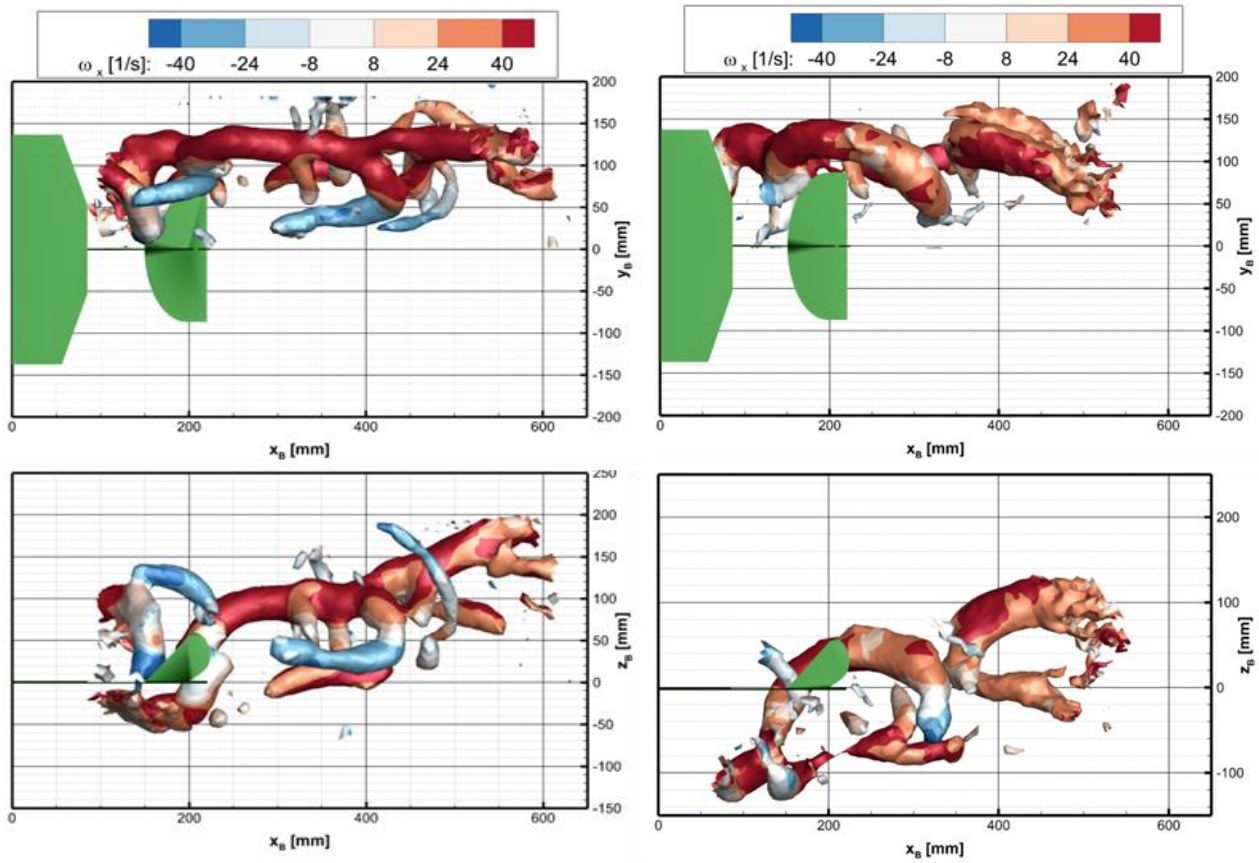

Fig. 15. Top and side views of the wake structures visualized by isosurfaces of Q=600 and colored by ω_x for phases II of configurations B (right) and C (left)

and only the main structure, the tip vortex, can be clearly seen. The root vortex is one of the structures that are not visible for configuration C while there are well defined for configuration B.

The dynamic motion of the DelFly during free-flight tests is inevitable, as DelFly is flying around a set point with small deviations from it. The largest deviations are found in the lateral direction which can reach a variation of 20 cm. Using the information from the flight tracking system, the position deviations are corrected for, in order to be able to process the data with the phase-lock averaging procedure. However, the motion of the DelFly, especially the lateral component which also involves the heading of the Delfly with respect to the free stream, changes the position and the orientation of the wake and to some extent the way the vortex structures are shed. This translates in the end in fluctuations of the position of the individual wake structures that causes the smaller structures to be spread out over the volume, so they are no longer detectable. The big structures are still visible but the core, as seen in figure 15, is larger due to this "blurring" of the vortex and the x-vorticity reached is smaller than for tethered conditions. The overall shape of the tip vortex however is still very similar to the vortex structure found in tethered conditions, indicating that the structures generated on both cases follow the same trend. However further research needs to be done to elaborate more detailed conclusions.

4 Conclusions

A large-scale volumetric flow visualization of a flapping-wing Micro Air Vehicle was performed using Robotic Co-axial Volumetric Velocimetry in combination with Helium Filled Soap Bubbles as tracers, with a total measurement volume of about $0.06\ m^3$. A phase-averaging procedure was applied to extract the wake structure at different phases along the flapping cycle. Experiments were carried out for different flight configurations, and for tethered and free flying conditions. The main vortex structures generated by the flapping-wing MAV have been identified and analyzed. The influence of the acceleration region has proven to be important, so Taylor's hypothesis is not valid. The flight parameters (U_∞, f_{flap} and α_b), that relate to a certain reduced frequency, alter considerably the vortex structures interaction changing the final topology of the wake.

References

[1] Armanini, S. F., Caetano, J. V., Croon, G. C. H. E. D., Visser, C. C. D., & Mulder, M. (2016). *Quasi-steady aerodynamic model of clap-and-fling flapping MAV and validation using free-flight data*. Bioinspiration and Biomimetics, 11(4). https://doi.org/10.1088/1748-3190/11/4/046002

[2] Bomphrey, R. J., Henningsson, P., Michaelis, D., & Hollis, D. (2012). *Tomographic particle image velocimetry of desert locust wakes: instantaneous volumes combine to reveal hidden vortex elements and rapid wake deformation*. Journal of The Royal Society Interface, 9(77), 3378–3386. https://doi.org/10.1098/rsif.2012.0418

[3] Bomphrey, R. J., Taylor, G. K., Lawson, N. J., & Thomas, A. L. (2006). *Digital particle image velocimetry measurements of the downwash distribution of a desert locust Schistocerca gregaria*. Journal of The Royal Society Interface, 3(7), 311-317. https://doi.org/10.1098/rsif.2005.0090

[4] Cheng, B., Tobalske, B. W., Powers, D. R., Hedrick, T. L., Wethington, S. M., Chiu, G. T. C., & Deng, X. (2016). *Flight mechanics and control of escape manoeuvres in hummingbirds*. I. Flight kinematics. The Journal of Experimental Biology, 219(22), 3518–3531. https://doi.org/10.1242/jeb.137539

[5] Clercq, K. D., & Kat, R. D. (2009). *Flow visualization and force measurements on a hovering flapping-wing MAV'DelFly II'*. Proc. 39th AIAA Fluid Dynamics Conference (June), 1–10. https://doi.org/10.2514/6.2009-4035

[6] Croon, G. C. H. E., Perçin, M., Remes, B. D. W., Wagter, C., & Ruijsink, R. (2016). *The DelFly: Design, aerodynamics, and artificial intelligence of a flapping wing robot*. https://doi.org/10.1007/978-94-017-9208-0

[7] Groen, M., Bruggeman, B., Mark Groen, Bart Bruggeman, Bart Remes, Rick Ruijsink, Bas van Oudheusden, H. B., & Remes, B. (2010). *Improving flight performance of the flapping wing MAV DelFly II*. Int. Micro Air Vehicle

[8] Gutierrez, E., Quinn, D. B., Chin, D. D., & Lentink, D. (2016). *Lift calculations based on accepted wake models for animal flight are inconsistent and sensitive to vortex dynamics*. Bioinspiration & biomimetics, 12(1), 016004.

[9] Jux, C., Sciacchitano, A., Schneiders, J. F. G., & Scarano, F. (2018). *Robotic volumetric PIV of a full-scale cyclist*. Experiments in Fluids, 59(4). https://doi.org/10.1007/s00348-018-2524-1

[10] Karasek, Matej & Percin, Mustafa & Cunis, Torbjørn & Oudheusden, Bas & De Wagter, Christophe & Remes, Bart & Croon, Guido. (2016). *First free-flight flow visualisation of a flapping-wing robot*.

[11] Muijres, F. T., Elzinga, M. J., Melis, J. M., & Dickinson, M. H. (2014). *Flies evade looming targets by executing rapid visually directed banked turns*. Science, 344(6180), 172 LP-177.

[12] Percin, M., Oudheusden, B. W. V., Croon, G. C. H. E. D., & Remes, B. (2016). *Force generation and wing deformation characteristics of a flapping-wing micro air vehicle "DelFly II" in hovering flight*. Bioinspiration and Biomimetics, 11(3). https://doi.org/10.1088/1748-3190/11/3/036014

[13] Percin, M., van Oudheusden, B. W., Eisma, H. E., & Remes, B. D. W. (2014). *Three-dimensional vortex wake structure of a flapping-wing micro aerial vehicle in forward flight configuration*. Experiments in fluids, 55(9), 1806. https://doi.org/10.1007/s00348-014-1806-5

[14] Sane, S. P. (2003). *The aerodynamics of insect flight*. Journal of experimental biology, 206(23), 4191-4208.

[15] Scarano, F. (2013). *Tomographic PIV: Principles and practice*. Measurement Science and Technology. Institute of Physics Publishing. https://doi.org/10.1088/0957-0233/24/1/012001

[16] Scarano, F., Ghaemi, S., Caridi, G. C. A., Bosbach, J., Dierksheide, U., & Sciacchitano, A. (2015). *On the use of helium-filled soap bubbles for large-scale tomographic PIV in wind tunnel experiments*. Experiments in Fluids, 56(2), 42.

[17] Schanz, D., Gesemann, S., & Schröder, A. (2016). *Shake-The-Box: Lagrangian particle tracking at high particle image densities*. Experiments in Fluids, 57(5). https://doi.org/10.1007/s00348-016-2157-1

[18] Schneiders, J. F. G., Scarano, F., Jux, C., & Sciacchitano, A. (2018). *Coaxial volumetric velocimetry*. Measurement Science and Technology. https://doi.org/10.1088/1361-6501/aab07d

[19] Spedding, G. R., Rosén, M., & Hedenström, A. (2003). *A family of vortex wakes generated by a thrush nightingale in free flight in a wind tunnel over its entire natural range of flight speeds*. Journal of Experimental Biology, 206(14), 2313–2344. https://doi.org/10.1242/jeb.00423

Copyright Statement